catalysts

Article

MXene/SiO_2-CeO_2 Nanoarchitectures for Photothermal-Catalytic Environmental Applications

Giusy Dativo [1,2,*], Javier Perez-Carvajal [1,*], Salvatore Scirè [2], Giuseppe Compagnini [2], Roberto Fiorenza [2,*] and Eduardo Ruiz-Hitzky [1]

[1] Materials Science Institute of Madrid (ICMM-CSIC), 28049 Madrid, Spain; eduardo@icmm.csic.es
[2] Department of Chemical Sciences, University of Catania, 95125 Catania, Italy; sscire@unict.it (S.S.); gcompagnini@unict.it (G.C.)
* Correspondence: giusy.dativo@phd.unict.it (G.D.); jperez@icmm.csic.es (J.P.-C.); rfiorenza@unict.it (R.F.)

Abstract

MXenes, a family of two-dimensional transition metal carbides and nitrides, exhibit exceptional electrical conductivity, tunable surface chemistry, and strong broadband light absorption. However, their practical implementation is often limited by structural instability, such as restacking and surface oxidation. In this study, we propose a strategy for the design of hybrid nanocomposites based on exfoliated $Ti_3C_2T_x$ MXene embedded within a porous silica (SiO_2) matrix and further functionalized with cerium dioxide (CeO_2) nanoparticles. The SiO_2 matrix, synthesized via a sol–gel approach, ensures homogeneous dispersion, increased porosity, and thermal stability, effectively reducing MXene restacking. Simultaneously, CeO_2 nanoparticles create surface oxygen vacancies and enhance interfacial reactivity. Comprehensive structural, morphological, surface, and optical characterizations confirm the formation of stable, light-responsive nanoarchitectures with tailored textural properties. Furthermore, the obtained material exhibit promising photothermal-catalytic properties. This work offers a materials-oriented approach for engineering multifunctional MXene-based architectures with enhanced photothermal performance, exemplified by their potential application in the photothermo-catalytic CO_2 conversion into solar fuels, showcasing the broader possibilities enabled by these materials.

Keywords: MXenes; CO_2 reduction; solar fuels; photothermo-catalysis

1. Introduction

The development of next-generation materials for energy and environmental technologies increasingly relies on the design of low-dimensional nanostructures with tailorable surface chemistry, tunable porosity, and high physicochemical stability [1]. Two-dimensional (2D) materials have garnered significant attention due to their unique physicochemical properties, such as large specific surface area, adjustable electronic structure, and excellent catalytic performance [2]. Among these, 2D transition metal carbides and nitrides, commonly referred to as MXenes, which were discovered in the past decade at Drexel University (by Gogotsi's team) [3,4], have attracted growing attention due to their layered structure, metallic conductivity, high specific surface area, and strong light absorption across the ultraviolet–near-infrared (UV–NIR) spectrum [5–7]. Their general formula, $M_{n+1}X_nT_x$ (where M is an early transition metal (e.g., Ti, V, Nb, Mo), X is carbon and/or nitrogen, and T_x represents surface terminations such as –OH, –O, or –F) allows extensive chemical tuning, enabling MXenes to interface with a wide range of matrices and guest

Check for updates

Academic Editor: Bo Weng

Received: 12 December 2025
Revised: 3 January 2026
Accepted: 7 January 2026
Published: 1 February 2026

https://doi.org/10.3390/catal16020136

materials [6,8]. MXenes combine metallic conductivity comparable to that of graphene, with the hydrophilicity typically observed in clays and layered double hydroxides, representing an unusual and highly advantageous combination of properties [6,9–11]. The first MXene, $Ti_3C_2T_x$, reported in 2011, showed metallic conductivity, which remains stable over a broad temperature range [12]. The MXenes are commonly synthesized via selective etching of the A-layer (typically Al or Si) from MAX phases ($M_{n+1}AX_n$) where n could be 1 or 2 and M stands for a transitional metal, while A represents an element from the IIIA or IVA groups, and X is representative of carbon and/or nitrogen [13,14], yielding a layered architecture with accessible surfaces and engineered interfacial chemistry [15]. Through selective etching of the A-layer, usually by chemical treatments involving fluoride-based solutions [16,17], the layered structure is preserved while exposing the transition metal carbide or nitride layers resulting in the formation of MXenes [18–20]. This top-down approach allows the retention of structural anisotropy and facilitates the introduction of surface terminations (–OH, –O, –F), which enhances the chemical reactivity and colloidal stability of MXenes in aqueous environments [21]. The abundance of surface functional groups, combined with their unique electronic and thermal properties, makes MXenes particularly attractive for catalysis under light and heat activation [22–25]. Despite these advantages, MXenes suffer from some drawbacks that hinder their practical application, notably rapid oxidation in air and restacking of individual layers, which severely reduces surface accessibility and reactivity [26,27]. These limitations can be effectively mitigated through nanoarchitecture engineering, such as incorporating MXenes into porous, thermally stable matrices that serve as barriers and structural supports. Although the oxidation of MXenes cannot be completely suppressed and may still occur over time, even within composite matrices, silica (SiO_2) is particularly attractive due to its chemical resilience, thermal stability, and high porosity, which improve MXene dispersion and accessibility of additional functionalities [28,29]. Its surface can be readily modified to enhance compatibility with a wide range of nanomaterials, including MXenes [30].

Our previous study has shown that embedding MXenes in porous and thermally stable silica-based frameworks can substantially slow down degradation and improve structural stability under ambient conditions [30]. In addition, MXenes exhibit broad-spectrum light absorption and excellent photothermal conversion efficiency, making them ideal candidates for photothermal catalysis [30–33].

This hybrid catalysis has emerged as a promising approach that combines the benefits of photocatalysis and thermocatalysis, simultaneously activating reactions via light-induced charge carriers and localized thermal effects [34,35]. This dual mechanism can improve reaction kinetics, lower the activation barrier, and promote product desorption, thus offering high selectivity and efficiency, especially under solar irradiation. It is particularly relevant for sustainable environmental processes such as CO_2 reduction, water splitting, and pollutant degradation [36–38]. Among these, CO_2 reduction plays a central role in carbon capture and utilization (CCU) strategies, enabling the conversion of emissions into valuable fuels and chemicals through sustainable catalytic processes [39–42]. The addition of metal oxides such as CeO_2 (ceria), to MXenes can significantly enhance their interfacial charge transfer properties by introducing oxygen vacancies and improving their photonic and electronic response [43]. CeO_2, as an unconventional rare earth photocatalyst [44], is also attractive due to its remarkable redox behavior, which can be exploited in various environmental applications, including the solar photothermo-catalytic CO_2 conversion [36,45–48].

In this context, we applied here a new route for the synthesis of MXene-based nanoarchitectures prepared from Ti_3AlC_2 MAX phase under mild etching conditions, using in situ–generated HF to promote a more sustainable approach [30]. The resulting multilayered MXene sheets were then modified by developing a SiO_2 matrix through cetyltrimethylammonium bromide (CTAB) intercalation intermediates [30], which facilitates the subsequent assembly of CeO_2 nanoparticles with the aim of improving their stability and photothermal properties. The microporous SiO_2 network was generated using a sol–gel process with tetramethyl orthosilicate (TMOS) as a precursor [28,49], while the CeO_2 nanoparticles were introduced via chemical precipitation [36]. In both cases, the SiO_2-CeO_2 formed a uniform, continuous coating on the MXene surface, stabilizing the structure against oxidation, partially preventing layered restacking, and improving light–material interactions. These MXene-based nanoarchitectures were designed to maximize surface accessibility and to exploit the synergistic effects between MXene and metal oxides in order to obtain composites with improved stability and photothermal features. This study represents an initial step toward the development of MXene-based nanoarchitectures for the production of solar fuels derived from CO_2, taking advantage of their inherent photothermal effects.

2. Results and Discussion

2.1. Preparation of MXene-Based Nanoarchitectures

The preparation of the MXene/SiO_2-$[CeO_2]_x$ nanoarchitectures begins with the selective etching of the Ti_3AlC_2 MAX phase. The X-ray diffractograms (XRD) patterns (Figure 1), collected in powder form, exhibit the characteristic reflections of this MAX phase, including a prominent (002) peak at 2θ = 9.62°, which corresponds to an interplanar spacing of approximately 0.92 nm. This value is consistent with the expected d-spacing for the (002) planes, given the lattice parameter $c \approx 1.86$ nm and $d_{(002)} \approx c/2 \approx 0.93$ nm, in agreement with the literature data [50]. After the mild etching, this peak shifts to a lower angle (2θ = 5.46°), indicating an increase in the interlayer spacing to approximately 1.62 nm and supporting the successful removal of Al, thus confirming the phase transformation into partially delaminated, multilayer $Ti_3C_2T_x$ MXene, as evidenced by the persistence of the (002) reflection, which indicates residual lamellar stacking rather than fully exfoliated single flakes. During this process, surface terminations, such as –OH, –O, and –F, are introduced, typically accompanying the Al etching and contributing to the structural delamination [50]. In addition to the main (002) reflection of $Ti_3C_2T_x$ MXene, weaker reflections at 2θ = 38.56° and 44.82° with d-spacings of 0.23 and 0.20 nm are observed, which can be ascribed to the (103) and (105) planes of residual MAX phase or to minor LiCl impurities arising from the LiF/HCl etching step [50]. These features indicate that a small fraction of incompletely etched material and/or salt residues remains, while the dominant phase corresponds to the partially delaminated $Ti_3C_2T_x$ MXene.

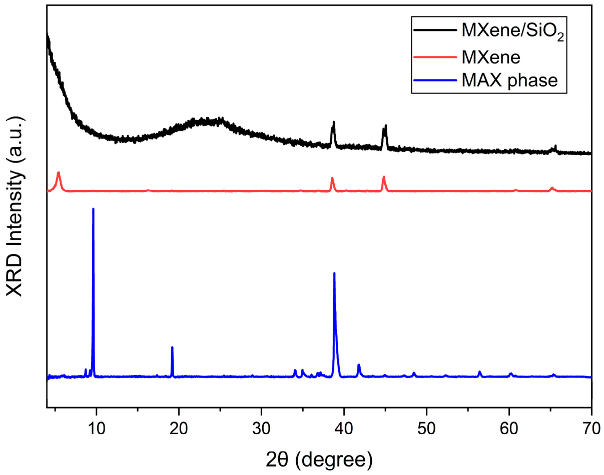

Figure 1. X-ray diffraction patterns showing the formation of MXenes after mild etching of the MAX phase and the subsequent formation of MXene/SiO_2 composites.

The XRD pattern of the MXene/SiO_2 composite exhibits attenuation of the (002) reflection of MXene, along with the emergence of a broad halo in the 20–30° 2θ region, attributed to the amorphous silica contribution. This behavior, in agreement with previous findings by Ruiz-Hitzky et al. [30] on analogous hybrids, indicates the disruption of the lamellar ordering and the effective dispersion of the silica phase within the layered MXene structure.

2.2. Structural, Textural, Optical, Morphological, and Surface Properties

The incorporation of SiO_2 into the system prevents the identification of the MXene phase in the nanoarchitecture by low-angle XRD, suggesting a certain loss of layer packing [30], while having minimal impact on the textural and optical properties. The low specific surface area (4.1 $m^2\ g^{-1}$) and total pore volume (0.015 $cm^3\ g^{-1}$) of the MAX phase reflects its non-porous compact layered structure (Table 1). After selective etching and partial delamination, the specific surface area increased to 10.4 $m^2\ g^{-1}$ in the $Ti_3C_2T_x$ MXene, as a result of partial exfoliation and the formation of interlayer voids (Table 1). The isotherm profile further points to the development of limited mesoporosity [51] (Figure S1). Upon incorporation of the SiO_2 matrix through sol–gel synthesis, the specific surface area increased markedly to 492.3 $m^2\ g^{-1}$ (Table 1, Figure S2), accompanied by a significant increase in pore volume (0.409 $cm^3\ g^{-1}$). The resulting N_2 physisorption isotherm can be classified as type IV with an H2 type hysteresis loop (Figure S2) as expected for mesoporous materials [51].

Table 1. Textural and optical properties of the examined samples.

Sample	BET Specific Surface Area ($m^2\ g^{-1}$)	Pore Volume ($cm^3\ g^{-1}$)	Pore Diameter (nm)	Band Gap (eV)
MAX (Ti_3AlC_2)	4.1	0.015	3.4	-
MXene ($Ti_3C_2T_x$)	10.4	0.039	3.4	2.61
MXene/SiO_2	492.3	0.409	3.8	2.76

This confirms that the silica scaffold mitigates further restacking of the expanded MXene sheets and promotes the formation of accessible mesoporous domains.

Ultraviolet-Visible Diffuse Reflectance Spectroscopy (UV-Vis DRS) measurements (Figures S3 and S4), performed to evaluate the optical band gap of the nanoarchitectures (Figure S4) as a function of binding energy [52], also show a significant difference compared to their pristine counterparts. It is important to highlight that the application of this method to composite materials requires some additional considerations. Indeed, as reported [52,53], the reflectance spectra of these samples are more complex compared to bare semiconductor oxides with homogenous crystalline phase, taking into account the absorption from the impurity phases present in this type of complex composites. Therefore, to extrapolate the Eg values also these features have been considered.

The optical band gap increases from 2.61 eV (MXene) to 2.76 eV (MXene/SiO_2, Table 1). This slight blue shift may be attributed to interfacial interactions between MXene sheets and the SiO_2 matrix, as well as possible confinement effects within the porous framework [30,54]. Given its metallic or semi-metallic nature, the MAX phase does not exhibit a significant band gap [55].

A detailed study on Transmission Electron Microscopy (TEM) (Figure 2) shows the morphologies of the materials during the different preparation steps. In Figure 2A, the MAX phase exhibits compact and dense aspect, characteristic of the non-etched precursor. The expanded MXene (Figure 2B), corresponding to a partially delaminated material, supporting the successful etching of the Al layers and the partial delamination of the $Ti_3C_2T_x$ sheets.

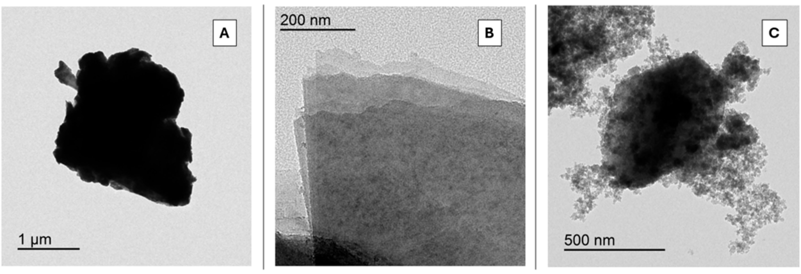

Figure 2. TEM images of (**A**) MAX phase; (**B**) MXene; and (**C**) MXene/SiO_2.

The transparent, sheet-like appearance indicates the formation of few-layer MXene nanosheets. During the synthesis, TMAOH was added after pH neutralization to further promote interlayer expansion prior to CTAB-assisted delamination, facilitating gallery widening and MXene dispersion without achieving complete exfoliation. As shown in the Scanning Electron Microscopy (SEM) image reported in the Figure S5A, partially stacked accordion-like domains coexist with regions of expanded galleries, consistent with the mild etching conditions used.

The MXene/SiO_2 nanoarchitecture (Figure 2C) exhibit a heterogeneous morphology with SiO_2 nanoparticles assembled to the surface of the MXene flakes, confirming the successful dispersion of partially delaminated MXene sheets within the silica matrix, resulting in a uniform nanostructure. The granular contrast and the surrounding lighter regions suggest a partial coverage of the MXene sheets by the silica phase, which is likely enhances the specific surface area and reactivity of these composite materials (SEM image in the Figure S5B).

TEM-EDX (Transmission Electron Microscopy-Energy Dispersive X-ray) semiquantitative elemental analysis (Table S1) reveals compositional changes occurring during the transformation from MAX phase to MXene and subsequent hybridization with SiO_2. In the MAX precursor, Ti and Al are present in almost stoichiometric amount (Ti: 50.0 at%; Al: 12.5 at%). Following selective etching, Al is substantially removed (3.02 at%), confirming the successful conversion to $Ti_3C_2T_x$. A prominent fluorine concentration (27.39 at%) is also observed, indicative of extensive surface termination via –F groups originating from the LiF/HCl etching solution. In the MXene/SiO_2 sample, the Si signal (24.47 at%) confirms the incorporation of the silica matrix. The Ti content is reduced, consistent with partial embedding or coverage of MXene flakes within the SiO_2 network. This is further supported by the simultaneous reduction in fluorine content (9.91 at%), suggesting a lower surface exposure of MXene domains. Overall, the EDX data support the formation of nanoarchitectures in which MXene layers are effectively dispersed and stabilized within a porous SiO_2 framework, in agreement with TEM images, BET surface area analysis, and XRD results. These compositional shifts not only validate the structural integration of MXene within the silica framework but also suggest potential enhancements in its functional performance. The high fluorine termination density may contribute to improved hydrophilicity and electrochemical activity, while the silica matrix offers mechanical stability and thermal resistance. Together, these features make the MXene/SiO_2 hybrid a promising candidate for applications in energy storage, catalysis, and sensing technologies.

Upon in situ growth of ceria within the MXene/SiO_2 matrix, XRD patterns (Figure 3) display weak reflections at $2\theta \approx 28.6°$, $33.1°$, and $47.5°$, assigned to the (111), (200), and (220) planes of fluorite CeO_2, respectively, confirming the formation of crystalline ceria (SEM images reported in the Figure S6). A zoomed view of the low-angle region (Figure S7) shows that the MXene (002) reflection is retained, although broadened and partially overlapped in all MXene/SiO_2-$[CeO_2]_x$ samples, indicating preservation of the $Ti_3C_2T_x$ framework after

SiO_2 and CeO_2 incorporation. No additional peaks attributable to crystalline TiO_2 phases are detected within the sensitivity of our measurements.

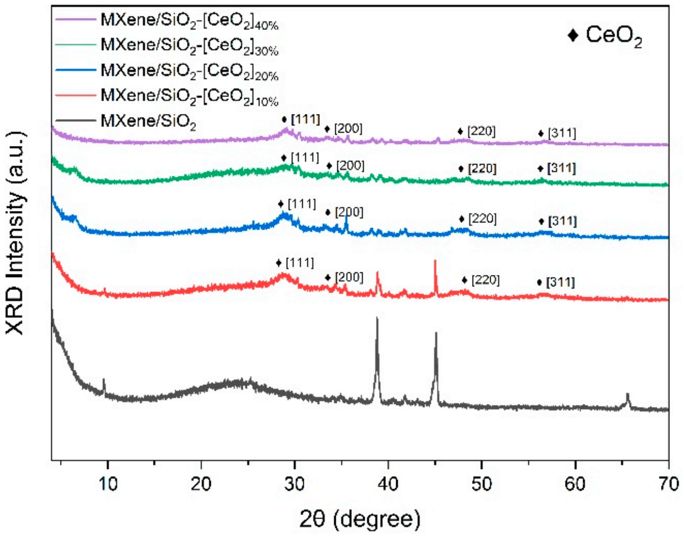

Figure 3. XRD patterns of MXene/SiO_2-CeO_2 composites.

Increasing CeO_2 content results in a marked reduction in specific surface area and pore volume (Table 2), likely due to substantial pore blockage by ceria nanoparticles. The BET specific surface area drops from 37.3 m^2 g^{-1} at 10 wt% CeO_2 to just 4.1–5.1 m^2 g^{-1} at 30–40 wt% CeO_2, indicating progressive pore occlusion. Nevertheless, all samples retain mesoporous characteristics, with average pore diameters around 3.8 nm. Simultaneously, the optical band gap slightly decreases from 2.76 eV (MXene/SiO_2, Table 1) to 2.63 eV (MXene/SiO_2-$[CeO_2]_{40\%}$), suggesting improved visible-light absorption. This band-gap narrowing is consistent with the incorporation of Ce^{3+} surface states and oxygen vacancies, which can lower the effective band gap and enhance the UV–vis absorption [51,56–58].

Table 2. Optical and textural properties of the examined samples.

Sample	Specific Surface Area (m^2 g^{-1})	Pore Volume (cm^3 g^{-1})	Pore Diameter (nm)	Band Gap (eV)
MXene/SiO_2-$[CeO_2]_{10\%}$	37.3	0.121	3.8	2.72
MXene/SiO_2-$[CeO_2]_{20\%}$	16.9	0.07	3.4	2.70
MXene/SiO_2-$[CeO_2]_{30\%}$	4.1	0.011	3.8	2.65
MXene/SiO_2-$[CeO_2]_{40\%}$	5.1	0.015	3.8	2.63
SiO_2-$[CeO_2]_{20\%}$	3.4	0.011	3	2.91

TEM of MXene/SiO_2-$[CeO_2]_{10\%}$, selected as the most promising sample for potential photothermal-catalytic applications (vide infra) reveals in Figure 4A that the material exhibits the characteristic crumpled, multilayer morphology of expanded $Ti_3C_2T_x$ sheets, partially embedded in the amorphous SiO_2 matrix.

The overall structure appears to be representative of a porous material. In the higher magnification image (Figure 4B), well-dispersed nanoparticles, attributed to CeO_2, are clearly distinguishable and uniformly distributed across the MXene/SiO_2 surface, considering also the reported morphology of the MXene/SiO_2 surface previously investigated [30] and the SEM and the TEM images reported here (Figures 2 and S5). Indeed, the morphology of the MXene/SiO_2 surface was characterized by MXene layers dispersed within a porous SiO_2 framework (Figures 2 and S5), therefore bearing in mind the very low amount of CeO_2

nanoparticles compared to the MXene/SiO_2 support and their lower size, the nanoparticles dispersion can be reasonably assigned to the presence of cerium oxide.

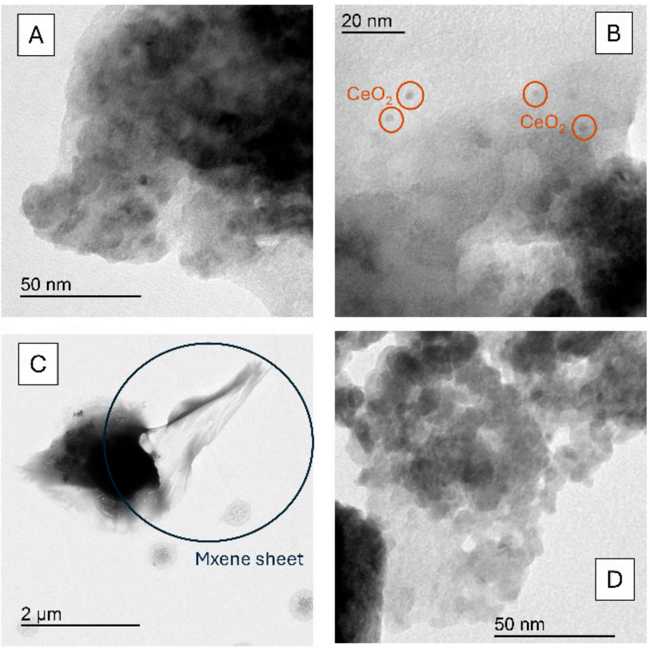

Figure 4. TEM images of MXene/SiO_2-$[CeO_2]_{10\%}$ at different magnification. In particular, (**A**) morphology of the MXene/SiO_2-$[CeO_2]_{10\%}$, (**B**) magnification on the CeO_2 nanoparticles, (**C**) MXene sheet highlighting, (**D**) other magnification for the CeO_2 nanoparticles.

This dispersion is further confirmed in Figure 4C and in Figure S6 by SEM analysis, where CeO_2 nanoparticles decorate the edges and basal planes of the MXene/SiO_2 surface, indicating effective interfacial contact between the diverse phases integrating the nanoarchitecture. Figure 4D provides a close-up view of these CeO_2 nanoparticles, revealing sizes in the range of about 3–7 nm and a quasi-spherical morphology. The intimate contact between CeO_2, SiO_2, and the MXene support is expected to enhance electron transfer processes and promote synergistic effects in catalytic applications.

The EDX spectrum from TEM examination corresponding to the semiquantitative elemental analysis table for the MXene/SiO_2-$[CeO_2]_{10\%}$ sample are presented in Table S2. The EDX analysis clearly reveals the elemental composition of the sample. These results confirm the successful synthesis and elemental composition of the MXene/SiO_2-$[CeO_2]_{10\%}$ sample. Furthermore, this morphological analysis combined with the data of the other characterization techniques strongly supports the deposition of cerium oxide on the MXene/SiO_2 surface.

A further confirmation was performed by elemental mapping by SEM-EDX. It revealed a homogeneous distribution of Ti, Ce, Si, and O across the MXene-based samples functionalized with CeO_2 and SiO_2 (Figures S8 and S9). Ti is mainly associated with the MXene sheets, forming the structural backbone; Ce is well dispersed, confirming successful CeO_2 deposition; Si and O correspond to the silica phase, likely coating or forming amorphous components. C is uniformly present, reflecting the composition of the MXene matrix, along with minor artifacts likely caused by the sample holder used during SEM preparation. No significant elemental segregation or clustering was observed, supporting the effective synthesis and integration of the diverse inorganic components.

The formation of the MXene/SiO_2-CeO_2 nanoarchitectures was further examined by Raman spectroscopy (Figure S10). The MAX phase exhibits bands at 269, 423, and 613 cm^{-1}, assigned to the E_{1g} and A_{1g} modes of Ti_3AlC_2 and the E_{2g} mode of its C sub-lattice [59,60]. After etching, these bands broaden and shift, in agreement with the transformation into

$Ti_3C_2T_x$ MXene, and the D and G bands of graphitic carbon at 1358 and 1585 cm^{-1} become more intense [61]. Upon addition of SiO_2, a broad band in the 670–1130 cm^{-1} region appears, attributed to Si–O and Si–O–Si vibrations [62], together with further broadening of the MXene D and G bands. In MXene/SiO_2-$[CeO_2]_{10\%}$, an additional band at ~460 cm^{-1} is observed, corresponding to the F_{2g} mode of fluorite CeO_2 [63], while the carbon D and G features remain detectable. These results confirm that the $Ti_3C_2T_x$ framework is still present after SiO_2/CeO_2 incorporation, and that the very weak signals of low-angle MXene reflections in XRD (Figures 3 and S7) is mainly due to the loss of long-range lamellar order rather than complete oxidation.

Finally, XPS analysis of the MXene/SiO_2 and MXene/SiO_2-$[CeO_2]_{10\%}$ before and after the photothermo-catalytic test has been performed in order to obtain information about the surface composition of the composites. In all the samples in the Si 2p binding energy region (Figure S11A) it is evident a broad peak centered at 102.4 eV consistent with the Si 2p levels of SiO_2 [64].

In the Ti 2p region (Figure S11B) the first component (yellow) is attributed, on the basis of the literature, to Ti atoms linked to termination groups (Ti–C; F–Ti–C), whereas a negligible amount of surface Ti oxidated species can be associated with the second component at about 460 eV [65]. Interestingly, in the MXene/SiO_2-$[CeO_2]_{10\%}$ the sharp peak position of Ti $2p_{3/2}$ at 455.6 eV present also in the MXene/SiO_2-$[CeO_2]_{10\%}$ after test, is at higher binding energy than that of bare MXene/SiO_2 (454.4 eV); a further indication of the successful formation of a composite with CeO_2 [45,65].

Ce 3d (Figure S11C) is split in 10 components due to the different Ce 4f level occupancies in the final state. Six of these components are assigned to Ce (IV) and four are attributed to Ce (III) [66]. The fresh sample contains mainly Ce (IV) with a small presence of Ce (III) (ca. 2% of the total amount of Ce). After photothermo-catalytic reaction, the amount of Ce (III) increases notably, reaching 15% of the total content of cerium. This demonstrated that during the photothermo-catalytic reaction the amount of oxygen vacancies of cerium oxide increased, allowing us to exploit its redox properties promoted by the photothermo-catalysis, to favor the CO_2 adsorption/activation process [36,38].

2.3. Photothermal Features and Photothermo-Catalytic Activity in the Solar CO_2 Conversion into Solar Fuels

Photothermal heating under NIR laser and simulated sunlight (Table 3) revealed efficient light-to-heat conversion across all MXene/SiO_2-$[CeO_2]_x$ samples. While the pristine MAX phase showed negligible heating under laser irradiation (T = 8 °C), MXene and MXene/SiO_2 exhibited substantial temperature increases (T = 228 °C and 258 °C, respectively), confirming their strong NIR absorption thanks to the presence of MXene (Figure S12). Interestingly, the incorporation of CeO_2 modified the photothermal response: MXene/SiO_2-$[CeO_2]_{10\%}$ exhibited the highest solar-induced temperature increase (T = 125 °C) (Figure S13), suggesting synergistic effects between the components. However, increasing CeO_2 loading led to a gradual decline in photothermal efficiency, possibly due to diverse factors such as reduced light penetration, decreased specific surface area, and partial coverage of the photoactive MXene surface by the CeO_2 nanoparticles.

To evaluate the photothermo-catalytic properties of the present nanoarchitectures, tests were carried out to assess the materials performance in solar photothermo-catalytic CO_2 conversion at 100 °C, using water vapor as a reducing agent (Figure S14A). Under the used experimental conditions, only CO and CH_4 were produced after 5 h of combined heating and simulated solar irradiation, operating in batch mode (Figure 5).

Table 3. Photothermal response of the samples under NIR laser and simulated solar irradiation. The T reported in the table is the temperature reached by the sample after 2 min of laser or solar lamp irradiation (experimental details reported in the Section 3.3).

Sample	Solar Lamp T (°C)	Laser T (°C)
MAX phase	117	8
MXene	114	228
MXene/SiO_2	121	258
MXene/SiO_2-$[CeO_2]_{10\%}$	125	201
MXene/SiO_2-$[CeO_2]_{20\%}$	103	161
MXene/SiO_2-$[CeO_2]_{30\%}$	101	122
MXene/SiO_2-$[CeO_2]_{40\%}$	96	116
SiO_2-$[CeO_2]_{20\%}$	110	18

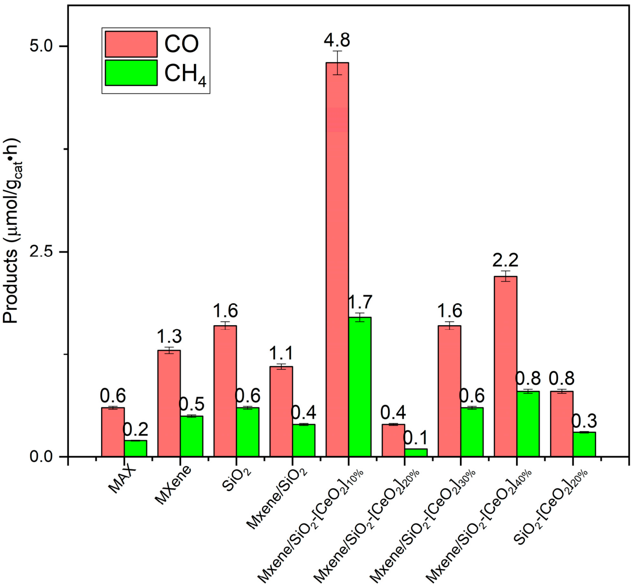

Figure 5. Photothermo-catalytic CO_2 conversion at T = 100 °C after 5 h of simulated solar irradiation on the investigated samples (experimental details reported in the Section 3.4).

Among the tested samples, MXene/SiO_2-$[CeO_2]_{10\%}$ exhibited the highest photothermo-catalytic activity (Figure 5), producing up to 4.8 μmol $g^{-1}{}_{cat}$ h^{-1} of CO and 1.7 μmol $g^{-1}{}_{cat}$ h^{-1} of CH_4 after 5 h of reaction.

The catalyst retained its structural features after the photothermo-catalytic test, as shown in the post-reaction XRD pattern (Figure S15). These findings, together with the Raman results and the previous literature [67,68], confirm that the thermal stability of $Ti_3C_2T_x$ can be significantly enhanced through incorporation into oxide-containing nanoarchitectures.

The performance of the MXene/SiO_2-$[CeO_2]_{10\%}$ is significantly enhanced compared to the pristine MXene or the CeO_2-free MXene/SiO_2 counterpart, demonstrating the synergistic role of CeO_2 in promoting CO_2 activation and enhancing charge separation. The photothermal properties of CeO_2 were efficiently activated only at low amount (10 wt%), indeed at higher CeO_2 loadings (20 wt%), the catalytic activity significantly decreased, whereas a little increase in activity was detected on the MXene/SiO_2-$[CeO_2]_{30\%}$ and MXene/SiO_2-$[CeO_2]_{40\%}$ compared to the MXene/SiO_2-$[CeO_2]_{20\%}$. Reasonably, only a little content of CeO_2 deposited on the MXene/SiO_2 surface led to promote efficient interactions between the components of the composite, whereas at high amounts only a partial combination of the photothermal activity of the single materials was exploited to convert the CO_2. In particular, an increase in the ceria content (20 wt%) favored probably a pronounced embedding of CeO_2 into the SiO_2 matrix, suppressing the photothermal features of the

MXene. Therefore, the catalytic performance of the MXene/SiO_2-$[CeO_2]_{20\%}$ was even worse of the bare SiO_2-$[CeO_2]_{20\%}$ sample (Figure 5) due to the lack of interactions between the SiO_2-CeO_2 and the MXene that in this case acted as a detrimental component. The same photothermo-catalytic activity showed by the bare SiO_2 and the MXene/SiO_2-$[CeO_2]_{30\%}$ samples suggested that a further increase in the ceria loading led to a surface segregation of SiO_2, whereas with the addition of the 40 wt% of CeO_2, only the cerium oxide was the predominant surface-active phase. Indeed, the photothermo-catalytic activity in the CO_2 conversion of the MXene/SiO_2-$[CeO_2]_{40\%}$ was comparable to that of pristine CeO_2 previously reported using the same experimental setup [36]. These findings suggest that, at high CeO_2 content (>10% wt), the contribution of the MXene-SiO_2 component may be significantly reduced or even suppressed. For these reasons, no linear correlation was found between the increase in the CeO_2 content at higher amount of 10 wt% and the photothermo-catalytic activity.

The rate of the CO formation remained higher than that of CH_4 across all architectures tested, suggesting a predominant two-electron reduction pathway, as also confirmed in the literature under similar experimental conditions [36,38]. Control experiments using SiO_2-$[CeO_2]_{20\%}$ (without MXene) showed negligible activity as well as testing the bare MAX phase, confirming the essential role of MXene in efficient light absorption, thermal activity and compared to the MAX phase, higher metal conductivity that facilitated the electrons mobility and, therefore, the CO_2 reduction reaction [69,70], while SiO_2 provides structural stability [71] and CeO_2 promotes CO_2 adsorption/activation and electron transfer processes [47]. Therefore, after the adsorption of CO_2 in the basic sites of CeO_2, the photothermal features of the composite enable a low-temperature activation of the CO_2. This aspect is very promising, leading to obtain solar fuels with an energy efficient process, considering that the conventional thermo-catalytic process required temperature higher than 200 °C [72]. Therefore, thanks to the combination of the photothermal features of the composite and the solar photothermo-catalytic approach at 100 °C, the CO_2 was converted into solar fuels using the photoelectrons generated in the conduction band of CeO_2 after solar light absorption and the protons formed by the holes in the CeO_2 valence band by the water vapor oxidation.

$Ti_3C_2T_x$ acts both as an efficient photothermal promoter, owing to its strong light-to-heat conversion capability and high electronic conductivity, and as an electron-transfer mediator that facilitates charge mobility at the MXene/CeO_2 interfaces. Localized photothermal heating induced by $Ti_3C_2T_x$ enhances the thermally activated steps of the reaction, while its conductive surface promotes electron transport and suppresses carrier recombination in CeO_2 [47].

$Ti_3C_2T_x$ was selected among MXenes because of its well-established synthesis, high stability, excellent photothermal efficiency, and strong interfacial interaction with both silica and ceria, which collectively enable a more efficient activation of CeO_2 than would be expected with other MXene compositions.

These results highlight the potential of these novel MXene-based nanoarchitectures for advancing photothermo-catalytic environmental applications.

3. Materials and Method

3.1. Materials

Ti_3AlC_2 MAX phase (200 mesh powder) was purchased from Shanghai Epoch Material Co. (Shanghai, China). The following chemical reagents were provided by Sigma-Aldrich (St. Louis, MO, USA) and used without further purification: tetramethyl orthosilicate (TMOS), lithium fluoride (LiF, analytical reagent grade), sodium hydroxide (NaOH, 97% purity, pellets), hydrochloric acid (HCl, 37.5 wt.%), cetyltrimethylammonium bromide

(CTAB, ≥98%), tetramethylammonium hydroxide (TMAOH, 25 wt.% in H_2O) and Cerium nitrate hexahydrate ($Ce(NO_3)_3·6H_2O$).

3.2. Catalysts Synthesis

3.2.1. Synthesis of MXene ($Ti_3C_2T_x$) Powder

MXene ($Ti_3C_2T_x$) was synthesized by adding 0.8 g of LiF to a 10 mL HCl solution 9 M under stirring for 30 min at room temperature. Subsequently, 0.25 g of MAX phase was added to the solution, and stirring was continued for 72 h at room temperature. The resulting mixture was neutralized by adjusting the pH with NaOH 11 M solution, followed by the addition of 4 mL of TMAOH and stirring for 1 h. This corresponds to the following molar ratio: MAX phase/LiF/HCl/TMAOH = 1:24:34:9. The suspension was centrifuged several times at 3500 rpm (RCF 1687× *g*) for 5 min each, washing the precipitate with deionized water. The collected powder was dried at 70 °C to obtain MXene powder.

Although drying of delaminated MXene may induce partial restacking, this step was required because the subsequent sol–gel synthesis of the SiO_2 matrix relies on alkoxysilanes that must react in organic media with controlled (stoichiometric or sub-stoichiometric) water content. Therefore, MXene was dried and redispersed in isopropanol as a pragmatic and reproducible approach to obtain the desired nanoarchitecture (see following section).

3.2.2. Synthesis of MXene/SiO_2 Composites

To prepare MXene-SiO_2, 400 mg of MXene was dispersed in 40 mL of deionized water and 40 mL of 7 mM CTAB solution, followed by stirring for 72 h at room temperature. The mixture was centrifuged at 3500 rpm (RCF 1687× *g*) for 10 min, and the precipitate was dried at 70 °C. The resulting MXene-CTAB composite was then dispersed in isopropanol.

The drying step was performed to obtain a reproducible and accurately weighed amount of MXene, as working directly with small volumes of the raw dispersion introduced significant uncertainties. For this reason, the resulting powder was redispersed.

Successively, a solution containing 355 µL of TMOS, 86.5 µL of deionized water, and 194 µL of methanol (i.e., in a 1:2:2 molar ratio) was added to the MXene-CTAB isopropanol dispersion, followed by stirring for 72 h at room temperature. To remove the CTAB template, the obtained gel was immersed in 40 mL of ethanol containing 4 mL of 1 M HCl, then heated at 70 °C for 24 h. The suspension was centrifuged at 3500 rpm (RCF 1687× *g*) for 10 min, and the collected precipitate was dried at 70 °C to yield MXene/SiO_2 as previously reported [30].

3.2.3. Synthesis of MXene/SiO_2-$[CeO_2]_x$ Nanoarchitectures

To prepare MXene/SiO_2 coated with cerium dioxide, 200 mg of MXene-SiO_2 was dispersed in deionized water along with $Ce(NO_3)_3·6H_2O$ (56 mg for 10 wt%, 126 mg for 20 wt%, 216 mg for 30 wt.% and 336 mg for 40 wt% CeO_2). These values were not based on a specific molar ratio between MXene/SiO_2 and Ce precursor, but were calculated to obtain nominal CeO_2 loadings of 10, 20, 30 and 40 wt% relative to MXene/SiO_2, assuming full conversion of the precursor into CeO_2 after calcination (corresponding to 0.129–0.774 mmol of $Ce(NO_3)_3·6H_2O$ per 200 mg of MXene/SiO_2).

The mixture was stirred for 3 h at 70 °C. Precipitation was induced by adding 1 M NaOH until the pH exceeded 7. The mixture was left to decant overnight, and the resulting precipitate was dried at 70 °C before being calcined at 300 °C for 2 h. The obtained samples were designated as MXene/SiO_2-$[CeO_2]_x$, where x represents the wt% of CeO_2. The obtained final samples were: MXene/SiO_2-$[CeO_2]_{10\%}$, MXene/SiO_2-$[CeO_2]_{20\%}$, MXene/SiO_2-$[CeO_2]_{30\%}$ and MXene/SiO_2-$[CeO_2]_{40\%}$.

3.2.4. Synthesis of SiO_2 and SiO_2-$[CeO_2]_x$ Composite Without MXene

SiO_2 matrices were prepared following the same procedure as for the MXene-SiO_2 synthesis, excluding the addition of MXene-CTAB. The obtained SiO_2 support was then coated with 20 wt% CeO_2 using the same methods described for MXene/SiO_2-$[CeO_2]_{20\%}$.

3.3. Characterization Techniques

Powder XRD were collected in a Davinci instrument from BRUKER (Billerica, MA, USA) in the range between 4 and 70 (2θ) angles. FE-SEM (Field Emission-SEM) images were recorded in a FEI NOVA NANOSEM 230 (Hillsboro, OR, USA) equipped with an EDAX-Ametek detector. TEM images and EDX analyses were obtained with a JEOL JEM-1400 Plus electron microscope (Akishima, Japan). Nitrogen adsorption isotherms at 77 K were recorded in an iSorb Anton Paar instrument (Graz, Austria) after outgassing the solid powder at 120 °C during 12 h under vacuum. The specific surface area of the solids was determined using the Brunauer—Emmett–Teller (BET) method, whereas the pore size distribution with the Barrett–Joyner–Halenda (BJH) model (from the desorption curves) with the help of ASiQwin Standard software 4.0 (Hiden Analytical Ltd., Warrington, UK). The UV–Vis DRS spectra were obtained with a JASCO V-670 (Hachioji, Japan). The optical band-gap (Eg) of the samples was estimated by plotting the modified Kubelka–Munk function vs. photon energy (hν) [52]. Raman spectra were obtained using a 532 nm laser in a μSense-LabC1X Enwave Optronics Raman Confocal equipment (Enwave Optronics Inc., Irvine, CA, USA). X-ray photoelectron spectroscopy analysis (XPS) was carried out on a K-Alpha™ + X-ray photoelectron spectrometer (Thermo Fisher Scientific, Waltham, MA, USA). The binding energy for the C (1s) peak at 284.9 eV (relative to adventitious carbon) was employed as reference.

To investigate the photothermal properties of the prepared MXene and MXene composites, the samples were irradiated with 808 nm wavelength laser light (830 mW) with a square beam of 0.3 cm × 0.3 cm and with a solar lamp (300 W, irradiance 10.7 mW/cm^2). The temperature was continuously recorded with an infrared thermal camera (HIKMICRO, Hangzhou, China) for laser irradiation and another one (SEFRAM, Saint-Étienne, France) for solar lamp irradiation for 2 min, then the light source was switched off until the temperature decreased to room temperature. The temperature was, therefore, evaluated after irradiation of the samples for two minutes. In particular, the powder samples were gently ground, and a small amount of each material was spread as a thin, homogeneous layer in a shallow sample holder, without any pressing or binder, so that the exposed surface was directly irradiated with the 808 nm laser or with the solar lamp.

3.4. Solar Photothermo-Catalytic CO_2 Conversion

The photothermo-catalytic performances of the selected materials were evaluated with preliminary tests using a cylindrical batch Pyrex reactor (volume = 275 mL) containing 0.120 g of catalyst. The sample was irradiated using the experimental set up reported in Figure S14A for 5 h using a solar lamp (Osram Ultra Vitalux 300 W, GmbH, Munich, Germany, irradiance 10.7 mW/cm^2, emission spectrum reported in the Figure S14B) placed inside a thermally insulated solar box. After lamp stabilization, the temperature inside the box reached 100 °C and was continuously monitored and controlled using an infrared thermal camera. Prior to simultaneous heating and irradiation, a mixture of CO_2 (purity 99.999%; impurities: $O_2 \leq 1$ ppm, $N_2 \leq 3$ ppm, $CO \leq 0.5$ ppm, $H_2O \leq 3$ ppm) and water vapor was introduced into the reactor to saturate the catalyst surface with reactant molecules. The initial CO_2 concentration was set at 2000 ppm. Water vapor was generated using a bubbler maintained at 80 °C. The flow rates of CO_2 and H_2O were regulated by mass flow controllers to achieve a molar ratio of 15, favoring CO_2 reduction over the competitive water splitting reaction [56]. Reaction products were then analyzed using an Agilent 8860 gas chromatograph (Santa Clara, CA, USA) equipped with a CARBOXEN-1000 column and a thermal conductivity detector (TCD), calibrated for the detection of carbon dioxide, methane and carbon monoxide. The detector was maintained at 200 °C, while the injector was set at 150 °C. Gas samples (1 mL) were collected from the reactor using a gastight syringe. The potential formation of other organic compounds was assessed using a Trace GC system (Thermo Fisher Scientific Inc., Waltham, MA, USA) with a Porapak Q column and a flame ionization detector (FID), using helium (He, 99.999%) as the carrier gas. All photothermo-catalytic experiments were carried out in triplicate, and the reported error bars represent the standard deviation of three independent measurements (typical relative error $\approx$ 3%).

4. Conclusions

In this study, nanoarchitectures based on exfoliated $Ti_3C_2T_x$ MXene embedded in a porous SiO_2 matrix and modified with CeO_2 nanoparticles were successfully developed to produce materials exhibiting photothermal responsiveness and retaining good stability. The sol–gel synthesis of the silica scaffold provided high specific surface area and mesoporosity, effectively mitigating MXene restacking and promoting homogeneous dispersion. Structural, surface and morphological characterizations confirmed the formation of a well-integrated composite, with TEM-EDX (Transmission Electron Microscopy) analysis showing uniform distribution of Ti, Si, C, and Ce elements throughout the material. Photothermal analysis demonstrated strong light-to-heat conversion under both NIR laser and simulated solar irradiation. While pristine MXene already showed excellent photothermal response, its performance was further enhanced by the incorporation of SiO_2 and an optimized CeO_2 loading. The MXene/SiO_2-$[CeO_2]_{10\%}$ sample achieved the highest temperature increase under both irradiation conditions, in agreement with a synergistic effect between the light-absorbing MXene substrate, the porous silica matrix, and the CeO_2 nanoparticles. These results underscore the potential of MXene-based nanoarchitectured materials as robust and tunable platforms for solar-to-thermal energy conversion. Their combination of high thermal response, structural integrity, and compositional versatility makes them promising candidates for future applications in solar-driven catalysis, sensing, and thermal management technologies.

Supplementary Materials: The following supporting information can be downloaded at: https://www.mdpi.com/article/10.3390/catal16020136/s1, Figures S1 and S2: N_2 adsorption and desorption isotherm of MXene and MXene/SiO_2 samples; Figures S3 and S4: UV-Vis-DRS spectra and Modified Kubelka–Munk function vs. binding energy for the estimation of the optical bandgap; Figures S5 and S6: SEM images; Tables S1 and S2: TEM-EDX analysis; Figure S7: Zoom of the XRD patterns of Figure 3; Figures S8 and S9: SEM image and corresponding EDX elemental maps of the MXene/SiO_2-$[CeO_2]_{10\%}$ sample; Figure S10: Raman spectra; Figure S11: XPS spectra; Figures S12 and S13: thermocamera images; Figure S14: Experimental set-up for the photothermo-catalytic conversion of CO_2; Figure S15: XRD patterns of the MXene/SiO_2-$[CeO_2]_{10\%}$ before and after the photothermo-catalytic test.

Author Contributions: G.D.: Investigation, Writing—original draft, Writing—review and editing. J.P.-C.: Writing—review and editing, Supervision, Methodology, Funding acquisition, Conceptualization. S.S.: Writing—review and editing, Resources. G.C.: Writing—review and editing, Resources. R.F.: Writing—review and editing, Supervision, Methodology, Conceptualization. E.R.-H.: Writing—review and editing, Supervision, Project administration, Methodology, Funding acquisition, Conceptualization. All authors have read and agreed to the published version of the manuscript.

Funding: This work was developed within the scope of the projects funded by the Agencia Estatal de Investigación MCIN/AEI/10.13039/501100011033, "ERDF A way of making Europe" (EU, project PID2022-137889OB-I00, RYC2022-037460-I; TED2021-131223B–I00). The authors also thank the Sicilian Micro and Nano Technology Research and Innovation Center (SAMOTHRACE project, CUP E63C22000900006) for the support.

Data Availability Statement: The data presented in this study are available on request from the corresponding author.

Acknowledgments: We acknowledge, Verónica Belmonte, Patricia Ferrer Alcaraz and Alba Pérez Cañaveras at "Servicios Técnicos de investigación", University of Alicante (Spain), for the assistance in the TEM & SEM images and EDX analyses. We also thank María Vizuete (ICMM-CSIC) and Elena Elvira for their technical assistance with sample management, as well as the Textural Characterization Facility at ICMM for their support.

Conflicts of Interest: The authors declare no conflicts of interest.

References

1. Solangi, N.H.; Karri, R.R.; Mubarak, N.M.; Mazari, S.A.; Azad, A.K. Emerging 2D MXenes as Next-Generation Materials for Energy Storage Applications. *J. Energy Storage* **2023**, *70*, 108004. [CrossRef]
2. Zeng, M.; Xiao, Y.; Liu, J.; Yang, K.; Fu, L. Exploring Two-Dimensional Materials Toward the Next-Generation Circuits: From Monomer Design to Assembly Control. *Chem. Rev.* **2018**, *118*, 6236–6296. [CrossRef]
3. Discussing MXenes with Yury Gogotsi. *Commun. Mater.* **2024**, *5*, 217. [CrossRef]
4. Naguib, M.; Kurtoglu, M.; Presser, V.; Lu, J.; Niu, J.; Heon, M.; Hultman, L.; Gogotsi, Y.; Barsoum, M.W. Two-Dimensional Nanocrystals Produced by Exfoliation of Ti_3AlC_2. *Adv. Mater.* **2011**, *23*, 4248–4253. [CrossRef] [PubMed]
5. Ronchi, R.M.; Arantes, J.T.; Santos, S.F. Synthesis, Structure, Properties and Applications of MXenes: Current Status and Perspectives. *Ceram. Int.* **2019**, *45*, 18167–18188. [CrossRef]
6. Naguib, M.; Mochalin, V.N.; Barsoum, M.W.; Gogotsi, Y. 25th Anniversary Article: MXenes: A New Family of Two-Dimensional Materials. *Adv. Mater.* **2014**, *26*, 992–1005. [CrossRef] [PubMed]
7. Gogotsi, Y. The Future of MXenes. *Chem. Mater.* **2023**, *35*, 8767–8770. [CrossRef]
8. Hong Ng, V.M.; Huang, H.; Zhou, K.; Lee, P.S.; Que, W.; Xu, J.Z.; Kong, L.B. Recent Progress in Layered Transition Metal Carbides and/or Nitrides (MXenes) and Their Composites: Synthesis and Applications. *J. Mater. Chem. A* **2017**, *5*, 3039–3068. [CrossRef]
9. Gogotsi, Y.; Anasori, B. The Rise of MXenes. *ACS Nano* **2019**, *13*, 8491–8494. [CrossRef]
10. Ruiz-Hitzky, E.; Ruiz-Garcia, C. MXenes vs. Clays: Emerging and Traditional 2D Layered Nanoarchitectonics. *Nanoscale* **2023**, *15*, 18959–18979. [CrossRef]
11. Ruiz-Hitzky, E.; Ruiz-Garcia, C.; Wang, X. MXenes and Clay Minerals in the Framework of the 2D Organic–Inorganic Hybrid Nanomaterials. *Chem. Mater.* **2023**, *35*, 10295–10315. [CrossRef]
12. Wei, Y.; Zhang, P.; Soomro, R.A.; Zhu, Q.; Xu, B. Advances in the Synthesis of 2D MXenes. *Adv. Mater.* **2021**, *33*, 2103148. [CrossRef]
13. Dahlqvist, M.; Barsoum, M.W.; Rosen, J. MAX Phases—Past, Present, and Future. *Mater. Today* **2024**, *72*, 1–24. [CrossRef]
14. Haftani, M.; Saeedi Heydari, M.; Baharvandi, H.R.; Ehsani, N. Studying the Oxidation of Ti_2AlC MAX Phase in Atmosphere: A Review. *Int. J. Refract. Met. Hard Mater.* **2016**, *61*, 51–60. [CrossRef]
15. Zhang, Z.; Duan, X.; Jia, D.; Zhou, Y.; Van Der Zwaag, S. On the Formation Mechanisms and Properties of MAX Phases: A Review. *J. Eur. Ceram. Soc.* **2021**, *41*, 3851–3878. [CrossRef]
16. Heidarpour, A.; Faraji, M.; Haghighi, A. Production and Characterization of Carbide-Derived-Nanocarbon Structures Obtained by HF Electrochemical Etching of Ti_3AlC_2. *Ceram. Int.* **2022**, *48*, 11466–11474. [CrossRef]
17. Wyatt, B.C.; Rosenkranz, A.; Anasori, B. 2D MXenes: Tunable Mechanical and Tribological Properties. *Adv. Mater.* **2021**, *33*, 2007973. [CrossRef]
18. Downes, M.; Shuck, C.E.; McBride, B.; Busa, J.; Gogotsi, Y. Comprehensive Synthesis of $Ti_3C_2T_x$ from MAX Phase to MXene. *Nat. Protoc.* **2024**, *19*, 1807–1834. [CrossRef]
19. Ghosh, A.; Pal, H.; Das, T.; Chatterjee, S.; Das, A. Synthesis and Characterization of MXene from MAX Phase. *Mater. Today Proc.* **2022**, *58*, 714–716. [CrossRef]
20. Paul, T.K.; Khaleque, M.D.A.; Ali, M.D.R.; Aly Saad Aly, M.; Bacchu, M.D.S.; Rahman, S.; Khan, M.D.Z.H. MXenes from MAX Phases: Synthesis, Hybridization, and Advances in Supercapacitor Applications. *RSC Adv.* **2025**, *15*, 8948–8976. [CrossRef]
21. Lee, A.; Shekhirev, M.; Anayee, M.; Gogotsi, Y. Multi-Year Study of Environmental Stability of $Ti_3C_2T_x$ MXene Films. *Graphene 2D Mater.* **2024**, *9*, 77–85. [CrossRef]

22. Xia, C.; Ye, H.; Kim, A.; Sabahi Namini, A.; Li, S.; Delbari, S.A.; Park, J.Y.; Kim, D.; Le, Q.V.; Varma, R.S.; et al. Recent Catalytic Applications of MXene-Based Layered Nanomaterials. *Chemosphere* **2023**, *325*, 138323. [CrossRef] [PubMed]
23. Yang, Y.; Xu, Y.; Li, Q.; Zhang, Y.; Zhou, H. Two-Dimensional Carbide/Nitride (MXene) Materials in Thermal Catalysis. *J. Mater. Chem. A* **2022**, *10*, 19444–19465. [CrossRef]
24. Pang, J.; Mendes, R.G.; Bachmatiuk, A.; Zhao, L.; Ta, H.Q.; Gemming, T.; Liu, H.; Liu, Z.; Rummeli, M.H. Applications of 2D MXenes in Energy Conversion and Storage Systems. *Chem. Soc. Rev.* **2019**, *48*, 72–133. [CrossRef] [PubMed]
25. Hamzehlouy, A.; Soroush, M. MXene-Based Catalysts: A Review. *Mater. Today Catal.* **2024**, *5*, 100054. [CrossRef]
26. Babar, Z.U.D.; Della Ventura, B.; Velotta, R.; Iannotti, V. Advances and Emerging Challenges in MXenes and Their Nanocomposites for Biosensing Applications. *RSC Adv.* **2022**, *12*, 19590–19610. [CrossRef]
27. Xie, Y.; Zhang, H.; Qu, Y.; Jiang, X.; Huang, J.; Zhang, X.; Gao, Y.; Tang, L.; Lv, Q.; Jiao, X.; et al. Unraveling the Ion-Accumulation-Induced Potential Limitations of MXene-Based Supercapacitors. *ACS Energy Lett.* **2025**, *10*, 345–355. [CrossRef]
28. Bonne, M.; Pronier, S.; Batonneau, Y.; Can, F.; Courtois, X.; Royer, S.; Marécot, P.; Duprez, D. Surface Properties and Thermal Stability of SiO_2-Crystalline TiO_2 Nano-Composites. *J. Mater. Chem.* **2010**, *20*, 9205. [CrossRef]
29. Wang, L.; Wang, Z.; Yang, H.; Yang, G. The Study of Thermal Stability of the SiO_2 Powders with High Specific Surface Area. *Mater. Chem. Phys.* **1999**, *57*, 260–263. [CrossRef]
30. Ruiz-Hitzky, E.; Ounis, M.; Younes, M.K.; Pérez-Carvajal, J. Silica–$Ti_3C_2T_x$ MXene Nanoarchitectures with Simultaneous Adsorption and Photothermal Properties. *Materials* **2024**, *17*, 4273. [CrossRef]
31. Guzelturk, B.; Kamysbayev, V.; Wang, D.; Hu, H.; Li, R.; King, S.B.; Reid, A.H.; Lin, M.-F.; Wang, X.; Walko, D.A.; et al. Understanding and Controlling Photothermal Responses in MXenes. *Nano Lett.* **2023**, *23*, 2677–2686. [CrossRef]
32. Zeng, W.; Ye, X.; Dong, Y.; Zhang, Y.; Sun, C.; Zhang, T.; Guan, X.; Guo, L. MXene for Photocatalysis and Photothermal Conversion: Synthesis, Physicochemical Properties, and Applications. *Coord. Chem. Rev.* **2024**, *508*, 215753. [CrossRef]
33. Li, R.; Zhang, L.; Shi, L.; Wang, P. MXene Ti_3C_2: An Effective 2D Light-to-Heat Conversion Material. *ACS Nano* **2017**, *11*, 3752–3759. [CrossRef] [PubMed]
34. Zhang, J.; Chen, H.; Duan, X.; Sun, H.; Wang, S. Photothermal Catalysis: From Fundamentals to Practical Applications. *Mater. Today* **2023**, *68*, 234–253. [CrossRef]
35. Ma, R.; Sun, J.; Li, D.H.; Wei, J.J. Review of Synergistic Photo-Thermo-Catalysis: Mechanisms, Materials and Applications. *Int. J. Hydrog. Energy* **2020**, *45*, 30288–30324. [CrossRef]
36. Dativo, G.; La Greca, E.; Liotta, L.F.; La Parola, V.; Condorelli, M.; Impellizzeri, G.; Compagnini, G.; Sciré, S.; Fiorenza, R. Solar Photothermo-Catalytic Conversion of CO_2 on Phyllosilicates Modified with Ni and CeO_2. *J. CO_2 Util.* **2024**, *82*, 102765. [CrossRef]
37. Fiorenza, R.; Calantropo, L.; La Greca, E.; Liotta, L.F.; Gulino, A.; Ferlazzo, A.; Musumeci, M.G.; Proietto Salanitri, G.; Carroccio, S.C.; Dativo, G.; et al. Solar-Promoted Photo-Thermal CO_2 Methanation on SiC/Hydrotalcites-Derived Catalysts. *Catal. Today* **2025**, *449*, 115182. [CrossRef]
38. Dativo, G.; Condorelli, M.; Compagnini, G.; Impellizzeri, G.; Scirè, S.; Fiorenza, R. CO_2 Conversion by Solar Photothermo Co-Catalysis on Montmorillonite-Based Catalysts. *Discov. Appl. Sci.* **2025**, *7*, 186. [CrossRef]
39. Mustafa, A.; Lougou, B.G.; Shuai, Y.; Wang, Z.; Tan, H. Current Technology Development for CO_2 Utilization into Solar Fuels and Chemicals: A Review. *J. Energy Chem.* **2020**, *49*, 96–123. [CrossRef]
40. Jeffry, L.; Ong, M.Y.; Nomanbhay, S.; Mofijur, M.; Mubashir, M.; Show, P.L. Greenhouse Gases Utilization: A Review. *Fuel* **2021**, *301*, 121017. [CrossRef]
41. Ghiat, I.; Al-Ansari, T. A Review of Carbon Capture and Utilisation as a CO_2 Abatement Opportunity within the EWF Nexus. *J. CO_2 Util.* **2021**, *45*, 101432. [CrossRef]
42. Chen, J.; Xu, Y.; Liao, P.; Wang, H.; Zhou, H. Recent Progress in Integrated CO_2 Capture and Conversion Process Using Dual Function Materials: A State-of-the-Art Review. *Carbon Capture Sci. Technol.* **2022**, *4*, 100052. [CrossRef]
43. Liu, Z.; Zhao, Y.; Li, S.; Sun, T.; Liu, H.; Wang, K.; Chen, X. $CeO_2/Ti_3C_2T_x$ MXene Nanostructures for Microwave Absorption. *ACS Appl. Nano Mater.* **2022**, *5*, 5764–5775. [CrossRef]
44. Gao, B.; Wang, Z.; Gao, T.; Yuan, S.; Yang, H.; Chen, C. Rare Earth Based Photocatalysts for Hydrogen Peroxide Production. *J. Rare Earths* **2025**, *43*, 405–416. [CrossRef]
45. Bellardita, M.; Fiorenza, R.; D'Urso, L.; Spitaleri, L.; Gulino, A.; Compagnini, G.; Scirè, S.; Palmisano, L. Exploring the Photothermo-Catalytic Performance of Brookite TiO_2-CeO_2 Composites. *Catalysts* **2020**, *10*, 765. [CrossRef]
46. Jang, M.; Choi, S.; Kim, Y.; Cha, J.; Kim, A.-R.; Jeong, H.; Kim, Y.; Hee Choi, S.; Woo Nam, S.; Lim, J.; et al. Effect of CeO_2 Redox Properties on the Catalytic Activity of Pt-CeO_x over Irreducible SiO_2 Support for Methylcyclohexane (MCH) Dehydrogenation. *Appl. Surf. Sci.* **2023**, *627*, 157134. [CrossRef]
47. Tran, D.P.H.; Pham, M.-T.; Bui, X.-T.; Wang, Y.-F.; You, S.-J. CeO_2 as a Photocatalytic Material for CO_2 Conversion: A Review. *Sol. Energy* **2022**, *240*, 443–466. [CrossRef]
48. Fiorenza, R.; Spitaleri, L.; Gulino, A.; Sciré, S. High-Performing Au-Ag Bimetallic Catalysts Supported on Macro-Mesoporous CeO_2 for Preferential Oxidation of CO in H_2-Rich Gases. *Catalysts* **2020**, *10*, 49. [CrossRef]

49. Aranda, P.; Belver, C.; Ruiz-Hitzky, E. Nanoarchitectures by Sol–Gel from Silica and Silicate Building Blocks. In *The Sol-Gel Handbook*; Wiley: Hoboken, NJ, USA, 2015; pp. 443–470, ISBN 978-3-527-33486-5.
50. Biswas, S.; Alegaonkar, P.S. MXene: Evolutions in Chemical Synthesis and Recent Advances in Applications. *Surfaces* **2021**, *5*, 1–34. [CrossRef]
51. Thommes, M.; Kaneko, K.; Neimark, A.V.; Olivier, J.P.; Rodriguez-Reinoso, F.; Rouquerol, J.; Sing, K.S.W. Physisorption of Gases, with Special Reference to the Evaluation of Surface Area and Pore Size Distribution (IUPAC Technical Report). *Pure Appl. Chem.* **2015**, *87*, 1051–1069. [CrossRef]
52. Makuła, P.; Pacia, M.; Macyk, W. How To Correctly Determine the Band Gap Energy of Modified Semiconductor Photocatalysts Based on UV–Vis Spectra. *J. Phys. Chem. Lett.* **2018**, *9*, 6814–6817. [CrossRef] [PubMed]
53. Landi, S.; Segundo, I.R.; Freitas, E.; Vasilevskiy, M.; Carneiro, J.; Tavares, C.J. Use and Misuse of the Kubelka-Munk Function to Obtain the Band Gap Energy from Diffuse Reflectance Measurements. *Solid State Commun.* **2022**, *341*, 114573. [CrossRef]
54. Taraghi, I.; Paszkiewicz, S.; Irska, I.; Pypeć, K.; Piesowicz, E. The Role of Interfacial Interactions on the Functional Properties of Ethylene–Propylene Copolymer Containing SiO_2 Nanoparticles. *Polymers* **2020**, *12*, 2308. [CrossRef]
55. Hadi, M.A. Superconducting Phases in a Remarkable Class of Metallic Ceramics. *J. Phys. Chem. Solids* **2020**, *138*, 109275. [CrossRef]
56. Karamian, E.; Sharifnia, S. On the General Mechanism of Photocatalytic Reduction of CO_2. *J. CO_2 Util.* **2016**, *16*, 194–203. [CrossRef]
57. Zhu, H.; Fu, X.; Zhou, Z. 3D/2D Heterojunction of CeO_2/Ultrathin MXene Nanosheets for Photocatalytic Hydrogen Production. *ACS Omega* **2022**, *7*, 21684–21693. [CrossRef]
58. Aktas, S.; Yildirim, Y.; Polat, O.; Sobola, D.; Sen, C.; Demiroglu, A.; Caglar, Y.; Caglar, M. Interplay between Iridium Doping and Oxygen Vacancies in Ceria: Experimental and Theoretical Investigation of Optical and Electronic Properties. *Ceram. Int.* **2025**, *51*, 34695–34715. [CrossRef]
59. Yoon, Y.; Le, T.A.; Tiwari, A.P.; Kim, I.; Barsoum, M.W.; Lee, H. Low Temperature Solution Synthesis of Reduced Two Dimensional Ti_3C_2 MXenes with Paramagnetic Behaviour. *Nanoscale* **2018**, *10*, 22429–22438. [CrossRef]
60. Sarycheva, A.; Gogotsi, Y. Raman Spectroscopy Analysis of the Structure and Surface Chemistry of $Ti_3C_2T_x$ MXene. *Chem. Mater.* **2020**, *32*, 3480–3488. [CrossRef]
61. Dixit, P.; Maiti, T. A Facile Pot Synthesis of (Ti_3AlC_2) MAX Phase and Its Derived MXene ($Ti_3C_2T_x$). *Ceram. Int.* **2022**, *48*, 36156–36165. [CrossRef]
62. Rong, J.; Haipeng, B.; Ijaz, M.F.; Shahzad, K.; Mushtaq, S.; Iqbal, Y. Multifunctional Magnetic SiO_2/Fe_3O_4@MXene Nanofiber Membranes for Reusable Removal of Doxorubicin and Organic Dyes from Industrial Wastewater. *Inorg. Chem. Commun.* **2025**, *182*, 115678. [CrossRef]
63. Balsamo, S.A.; La Greca, E.; Calà Pizzapilo, M.; Sciré, S.; Fiorenza, R. CeO_2-rGO Composites for Photocatalytic H_2 Evolution by Glycerol Photoreforming. *Materials* **2023**, *16*, 747. [CrossRef]
64. Calantropo, L.; La Greca, E.; Liotta, L.F.; Impellizzeri, G.; Gulino, A.; Ferlazzo, A.; Vitiello, L.; Carroccio, S.C.; Scirè, S.; Fiorenza, R. Solar Photothermo-Catalytic CO_2 Conversion into Methane: Effect of Phyllosilicates on the Performance of Ni-Zn-Al Layered Double Hydroxide-Derived Catalysts. *J. CO_2 Util.* **2026**, *103*, 103302. [CrossRef]
65. Ta, Q.T.H.; Tran, N.M.; Noh, J.-S. Rice Crust-Like ZnO/$Ti_3C_2T_x$ MXene Hybrid Structures for Improved Photocatalytic Activity. *Catalysts* **2020**, *10*, 1140. [CrossRef]
66. Bêche, E.; Charvin, P.; Perarnau, D.; Abanades, S.; Flamant, G. Ce 3d XPS Investigation of Cerium Oxides and Mixed Cerium Oxide ($Ce_xTi_yO_z$). *Surf. Interface Anal.* **2008**, *40*, 264–267. [CrossRef]
67. Arulanantham, R.R.; Savariraj, A.D.; Ragupathi, V. MXene-Metal Oxide Composites: Prospectus, Progress and Challenges as Anode Material for Lithium-Ion Batteries. *J. Alloys Compd.* **2025**, *1022*, 179761. [CrossRef]
68. Liu, N.; Li, Q.; Wan, H.; Chang, L.; Wang, H.; Fang, J.; Ding, T.; Wen, Q.; Zhou, L.; Xiao, X. High-Temperature Stability in Air of $Ti_3C_2T_x$ MXene-Based Composite with Extracted Bentonite. *Nat. Commun.* **2022**, *13*, 5551. [CrossRef]
69. Saha, D.; Dalmieda, J.; Patel, V. Surface-Modified MXenes: Simulation to Potential Applications. *ACS Appl. Electron. Mater.* **2023**, *5*, 2933–2955. [CrossRef]
70. Serafin, J.; Dziejarski, B.; Oindo Achieng, G.; Vendrell, X.; Chaitoglou, S.; Amade-Rovira, R. Comprehensive Analysis of MAX Phase and MXene Materials for Advanced Photocatalysis, Electrocatalysis and Adsorption in Hydrogen Evolution and Storage. *J. Ind. Eng. Chem.* **2025**, *142*, 18–33. [CrossRef]
71. Bawaked, S.; Narasimharao, K. Structural and Catalytic Properties of Copper Silicate Nanomaterials. *Sci. Rep.* **2020**, *10*, 518. [CrossRef] [PubMed]
72. Li, Y.; Chan, S.H.; Sun, Q. Heterogeneous Catalytic Conversion of CO_2: A Comprehensive Theoretical Review. *Nanoscale* **2015**, *7*, 8663–8683. [CrossRef] [PubMed]

https://doi.org/10.3390/catal16020136